Journal of Applied Mechanics Vol.12, pp.875-886 (August 2009) JSCE

Application of spatial integral models to water intrusion process into porous media and its verification

Bidur Ghimire*, Shinichiro Nakashima** and Takashi Hosoda***

* Ph.D. Student, Department of Urban Management, Kyoto University (C1-3, Kyodai-Katsura, Nishikyo-ku, Kyoto, 615-8540)
** Member Res. Associate, Pioneering Research Unit for Next Generation, Kyoto University (B104, Kyodai-Katsura, Kyoto, 615-8530)
*** Member Professor, Department of Urban Management, Kyoto University (C1-3, Kyodai-Katsura, Nishikyo-ku, Kyoto, 615-8540)

In this paper, we deal with the intrusion processes of laminar and turbulent flows into porous media lying on the horizontal plane. It is known that, based on the self-similarity analysis, the transient intrusion processes can be categorized into the inertia-pressure (IP) and the pressure-drag (PD) regimes. Temporal changes of water intrusion in both regimes are characterized by the power laws on time for the flow characteristics such as the front position, the depth at the inlet etc. We propose the spatial integral models using similarity function of depth and velocity distributions to analyze the flow from the initial stage to the final steady stage describing both the two flow regimes. The formulation to derive the ordinary differential equations of spatial integral models is firstly described, and then the basic characteristics of the spatial integral models are shown. It is shown from the numerical simulation that the IP regime appears in the initial stage and the PD regime follows it. We also carried out vertical 2D numerical simulations for the free surface flow inside the porous media using volume of fluid (VOF) method. The results of analytical integral models were compared with the results of numerical simulation and hydraulic experiments. The close agreement in the results proves the applicability of the formulation and also the algorithm adopted proves to be a promising tool for the numerical simulation of unsteady free surface flow through porous media.

Key Words : *porous media, integral model, unsteady free-surface flow, CIP method, VOF method*

1. Introduction

The free surface flow of an incompressible fluid through porous media has gained extensive attention due to its ever-broader range of practical applications. Ground water flow problems, geophysical systems, enhanced oil reservoir recovery, underground spreading of chemical waste and chemical catalytic reactors are a few examples of its applications. An important branch of porous media research involves the modeling of flow within the soil. Even though Darcy law has been used nearly exclusively in the studies of porous medium phenomena, there is considerable evidence that at high-velocity, the Darcy law does not hold in many subsurface systems. Any deviations from this linear relation may be defined as non-Darcy flow. The physical explanation of the non-linear deviation from Darcy's law is still an issue and is not completely known. Usually, Reynolds number is taken as a criterion for the demarcation of the flow regimes between laminar and turbulent. There is a smooth transition of flow from laminar to fully developed turbulent flow. In this study we considered the pore Reynolds number Re_p based on the mean diameter D of porous media and volume averaged interstitial velocity u_i i.e. $\mathrm{Re}_p = u_i D/\nu$; where ν is the kinematic viscosity of the fluid. The demarcation is considered[1)] as below,

(i) $\mathrm{Re}_p \leq 1$: creeping or Dacrian laminar regime
(ii) $1\sim10 < \mathrm{Re}_p < 500$: nonlinear laminar regime
(iii) $\mathrm{Re}_p \geq 500$: turbulent regime

According to the second criteria above, the Darcy law can still be applicable upto $\mathrm{Re}_p = 10$ without introducing significant error. These values represent a range of pore Reynolds number because a sharp demarcation of the different flow regimes in the porous media is impossible due to the gradual transition between them. If the flow is laminar the linear law of resistance is applicable i.e. hydraulic gradient is taken proportional to the fluid velocity and if the flow is turbulent, the hydraulic gradient is assumed proportional to the square of the velocity which is also called quadratic law of resistance for high velocity flow inside porous media. In this work,we deal with the unsteady intrusion of water into porous media consisting of large grain size, which can be applied to simulate the storm water storage into granular road sub-base from a side drain channel, under prescribed upstream boundary conditions as shown in Fig. 1. This in-site underground storage is receiving much interest in the sustainable urban drainage systems. The unsteady transient free-surface porous media flow model could be a potential decision tool to study various hydrological parameters quantitatively for such urban flood calculation.

The common fundamental equations for solid-liquid multiphase flows with the inertia force term, which is generally neglected in the conventional underground flows, are used as the basic model for this study because the pervious and granular road sub-base material consists of large grain size material and one can expect inertial flows through such strata. The fundamental characteristics of intrusion process are firstly investigated theoretically using the depth averaged equations with the local and convective inertia term and the porous drag resistance terms in the momentum equation. Assuming the self-similarity distributions of depth and velocity, the authors in their previous work have already derived the similarity law of intrusion process with entry velocity, the propagation of front

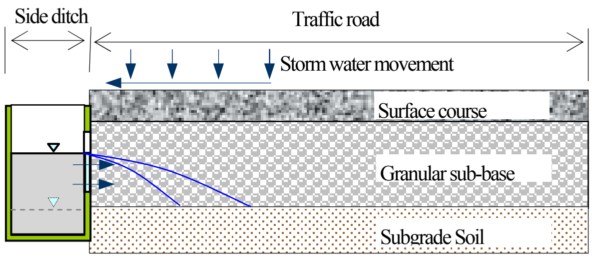

Fig. 1 Schematic diagram showing intrusion of storm water into porous sub-base from the side drain in a typical road section

position and the depth distribution under two different boundary conditions. In the abrupt unsteady intrusion process, the earlier inertia-pressure (IP) regime is gradually dominated by the non-inertial pressure-drag (PD) regime[2]. In this paper, we derive the spatial integral models incorporating the similarity functions of flow depth and velocity for both laminar and turbulent flows. It is pointed out that we can deal with both the IP regime and PD regime using the proposed models.

The results derived in this study are verified by carrying out the numerical simulations and hydraulic experiments. The vertical 2D numerical simulation is carried out by applying the finite volume method coupled with CIP-VOF technique to define the moving free surface. It is pointed out that the power law of propagation of front position, the distribution of depth, etc. can be reproduced in the results of simulations and hydraulic experiments.

2. Problem statement

In this section, we present the theoretical background about the current work along with the results of previous works[2] regarding the temporal power of depth, entry velocity and front positions. The results were derived by considering the similarity distributions. These results will be verified later from the results of integral model.

2.1 Theoretical considerations

The governing equations for the conservation of mass and momentum as given in the section 7 are taken as the basic equations for the unsteady free-surface flow through porous media. In order to investigate fundamental characteristics of intrusion process, the depth-averaged equations are used. The depth averaged continuity and momentum equations for one dimensional flow with inertia and drag resistance terms can be written as

$$\frac{\partial\{(1-C)h\}}{\partial t}+\frac{\partial\{(1-C)hU\}}{\partial x}=0 \tag{1}$$

$$\begin{aligned}&\frac{\partial\{(1-C)hU\}}{\partial t}+\frac{\partial\{(1-C)hU^2\}}{\partial x}\\&=-(1-C)gh\frac{\partial z_s}{\partial x}+\frac{\partial}{\partial x}\left\{(1-C)\frac{\tau_{xx}}{\rho}h\right\}-\frac{\tau_{bx}}{\rho}-\frac{R_x}{\rho}h\end{aligned} \tag{2}$$

where t is the time, x is the spatial coordinate, h is the flow depth, U is the depth averaged velocity, z_s is the free surface elevation, τ_{xx} is the viscous stress, τ_{bx} is the bottom shear stress and ρ is the density of water. For the analytical study, these stress terms are neglected due to their relative insignificance to the porous resistance term. The volumetric concentration of solid particles C is taken constant for the rigid porous media. The last term of Eq. (2) represents the resistance offered by the porous matrix. Hence for the analysis of flow in porous media where linear and quadratic resistance laws are applied separately, the resistance term is given by

$$\frac{R_x}{\rho}=\begin{cases}C_L U & \text{for laminar flow (linear law)}\\ C_T U|U| & \text{for turbulent flow (quadratic law)}\end{cases} \tag{3}$$

where C_L and C_T are the constant coefficients for linear and quadratic resistance terms respectively. The coefficients are considered to be dependent only on the characteristics of porous media in this study. The constant coefficients for linear and quadratic resistance laws can be written from the consideration of Darcy law and turbulent resistance given by

$$C_L=\frac{\nu(1-C)^2}{k} \tag{4}$$

$$C_T=\frac{(1-C)^3F_{ch}}{\sqrt{k}} \tag{5}$$

where ν is the kinematic viscosity of the fluid, F_{ch} is the Forchheimer's inertia coefficient and k the permeability in m^2 of the porous medium. For a rigid and isotropic porous media, the set of continuity and momentum equation can be written for the theoretical study as,

$$\frac{\partial h}{\partial t}+\frac{\partial hU}{\partial x}=0 \tag{6}$$

and

$$\frac{\partial U}{\partial t}+U\frac{\partial U}{\partial x}+g\frac{\partial h}{\partial x}=-\frac{R_x h}{\rho(1-C)} \tag{7}$$

2.2 Flow domain and boundary conditions

Two types of flow domains are considered for the study of intrusion dynamics of fluid into the porous media. In this study the two conditions are named as case A and case B. Case A [see Fig. 2(a)] represents the domain subjected to upstream pressure boundary whereas case B [see Fig. 2(b)] represents the domain subjected to upstream flux boundary.

For case A, a horizontal porous medium, which rests on an impermeable base, is considered and it is connected to a pool of water with a vertical flat gate at the origin as shown in the Fig. 2(a). Initially, the water is retained behind this vertical flat gate and to start the unsteady intrusion the gate at the origin (x = 0) is released

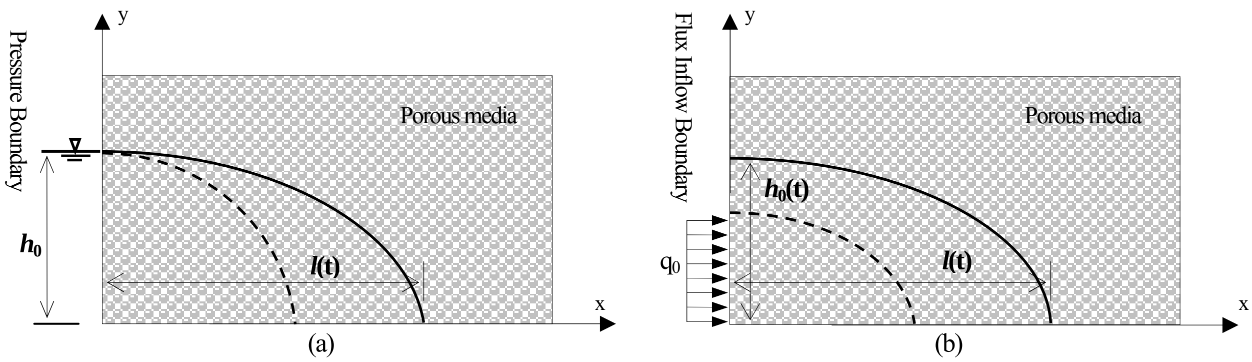

Fig. 2 Schematic diagrams showing flow domains subjected to constant upstream (a) water level h_0: case A and (b) inflow discharge q_0: case B.

instantaneously to give way to the water to intrude into the pore space being occupied by gas (air) of negligible viscosity, under the constant hydraulic head. Thus at the upstream boundary ($x = 0$), the hydraulic head in the pool remains constant with time i. e. the condition $h(x = 0, t > 0) = h_0$ is satisfied, where h_0 is the constant value of inlet water depth.

For case B i.e. when the upstream boundary of the domain is subjected to a constant prescribed inflow flux, the depth at the origin also varies with time as shown in Fig. 2(b). Thus in this case the condition $q(x = 0, t > 0) = q_0$ is satisfied, where q is the flux and q_0 is the constant value of inflow flux. In the subsequent section, we are interested in solving Eqs. (6) and (7) subject to aforementioned initial and boundary conditions.

2.3 Similarity transformation and power law solutions

The solutions for depth and velocity distributions are derived based on the assumed similarity of depth and velocity to clarify the fundamental characteristics of intrusion of water under two boundary conditions for both laminar and turbulent resistance laws. Only a brief explanation of previous work[2] is made here for clarity. The methods based on similarity transformation had been applied to the dam break flow of viscous fluid where temporal and spatial distribution of depth and velocity were derived analytically balancing the pressure gradient and viscous terms[3,4]. Among others Barenblat[5] used Boussinesq equation and Huppert[6] used Darcy equation as the basic governing equations for similarity transformation. The inertia term in the flow equation has been neglected in most of the reported literatures though we expect its significance in the porous media having high permeability value. Nonetheless, the similarity reduction is very useful, because it allows many interesting results to be obtained, for example regarding the position of front, its speed of propagation and some other nonlinear characteristics[7].

In this paper we derive the integral models applicable to all the flow regimes investigated using similarity functions. The distribution of entry velocity U_0, depth at origin h_0, and the front position l are expressed in terms of temporal powers a, b and c as given by

$$U_0 = \alpha V_0 \left(\frac{t}{T_0} \right)^a , h_0 = \beta L_0 \left(\frac{t}{T_0} \right)^b \text{ and } \quad l = \gamma L_0 \left(\frac{t}{T_0} \right)^c \qquad (8)$$

where α, β and γ are constant coefficients; V_0, L_0 and T_0 are the characteristic velocity, length and time scales respectively. These characteristic parameters are explained for each of the cases considered in the respective section. It will be shown that the power laws with respect to time given by Eq. (8) are inherited both with the Inertia-Pressure and Pressure-Drag regimes in the derived integral formulations. The similarity distributions of the depth $h(x, t)$ and velocity $U(x, t)$ are defined as

$$h = h_0 F(\xi) \text{ and } U = U_0 G(\xi) \qquad (9)$$

subject to

$$F(0) = 1 , F(1) = 0 , G(0) = U_0 \text{ and } G(1) = U_F \qquad (10)$$

where ξ is the similarity variable given by $\xi = x/l(t)$, U_F is the velocity at the front and the functions F and G are the non-dimensional similarity distribution functions for depth and velocity, respectively. These similarity functions for all the time steps are expressed as

$$G = 1\text{-}A\xi , \text{ and } F = 1\text{-}B\xi \qquad (11)$$

where A and B are constant coefficients to be determined using similarity law. We assume that these values do not change significantly for different flow regimes. Using these substitutions for G and F in the governing equations and after some simplification we have already derived A = -1.0, and B = 1.0 in our previous work[2].

(1) Pressure inlet boundary

This is the condition where upstream boundary is set as a constant water depth h_0. The characteristic time, length and velocity are defined as

$$T_0 = (h_0 / g)^{\frac{1}{2}} , \ L_0 = h_0 \text{ and } V_0 = (g h_0)^{\frac{1}{2}} \qquad (12)$$

The temporal powers a, b and c are determined using Eq. (9) and Eq. (12) in the transformed continuity and momentum equations. Each combination of transformed momentum equation such as Inertia-Pressure terms and Pressure-Drag terms are taken and solved for. The results are given in table 1.

Table 1. Summary of the temporal powers

Assumed resistance law	Case A (Pressure boundary)		Case B (Flux inflow boundary)	
	IP	PD	IP	PD
laminar	a=0 b=0 c=1	a=-1/2 b=0 C=1/2	a=0 b=0 c=1	a=-1/3 b=1/3 c=2/3
turbulent	a=0 b=0 c=1	A=-1/3 b=0 C=2/3	a=0 b=0 c=1	a=-1/4 b=1/4 c=3/4

(2) Flux inlet boundary

In this case the upstream boundary is set as a constant inflow flux q_0 which satisfies the condition $U_0(t)h_0(t) = q_0$ (constant) in which the depth at origin $h_0(t)$ and entry velocity $U_0(t)$ are the functions of time. The characteristic time, length and velocity are defined as

$$T_0 = \left(\frac{q_0}{g^2}\right)^{\frac{1}{3}}, \ L_0 = \left(\frac{q_0^2}{g}\right)^{\frac{1}{3}} \text{ and } V_0 = \left(gq_0\right)^{\frac{1}{3}} \tag{13}$$

Using Eqs. (9) and (13) the temporal powers a, b and c are obtained from the transformed continuity and momentum equation for both the inertia-pressure and pressure-drag regime. The summary of the results are presented in table 1.

3. Derivation of integral model for laminar flow

In this case the hydraulic gradient is assumed to be proportional to the linear power of velocity. For the flow with small Reynolds number, the resistance coefficient in Eq. (3) is given by Eq. (4). The governing momentum Eq. (7) into its conservative form with the help of continuity equation is given by

$$\frac{\partial hU}{\partial t} + \frac{\partial hU^2}{\partial x} + g\frac{\partial}{\partial x}\left(\frac{h^2}{2}\right) = -\frac{C_L hU}{(1-C)} \tag{14}$$

The governing Eqs. (4) and (14) can be integrated from $x = 0$ to $x = l(t)$ at any instant as

$$\int_0^{l(t)} \left[\frac{\partial h}{\partial t} + \frac{\partial hU}{\partial x}\right] dx = 0 \tag{15}$$

$$\int_0^{l(t)} \left[\frac{\partial hU}{\partial t} + \frac{\partial hU^2}{\partial x} + g\frac{\partial}{\partial x}\left(\frac{h^2}{2}\right)\right] dx = -\int_0^{l(t)} \left[\frac{C_L hU}{(1-C)}\right] dx \tag{16}$$

Further, using similarity distribution functions as expressed by Eq. (9) and on simplification using Leibnitz integral rule each term in Eqs. (15) and (16) can be simplified. For the compactness, the results after simplification for each terms of continuity and momentum are given in Eq. (17)

$$\left.\begin{aligned}
&\int_0^{l(t)} \frac{\partial h}{\partial t} dx = \frac{d}{dt}\int_0^{l(t)} h dx - h\big|_{x=l}\frac{dl}{dt} = \frac{d\left(h_0 l\right)}{dt}\int_0^1 F d\xi\,, \\
&\int_0^{l(t)} \frac{\partial hU}{\partial x} dx = -h_0\left(t\right)U_0(t)\ , \\
&\int_0^{l(t)} \frac{\partial hU}{\partial t} dx = \frac{d}{dt}\int_0^{l(t)} hU dx - (hU)\big|_{x=l}\frac{dl}{dt} \\
&\qquad = \frac{d\left(h_0 U_0 l\right)}{dt}\int_0^1 FG d\xi\ , \\
&\int_0^{l(t)} \frac{\partial hU^2}{\partial x} dx = -h_0 U_0^2\,, \\
&\int_0^{l(t)} \frac{\partial}{\partial x}\left(\frac{h^2}{2}\right) dx = -\frac{h_0^2}{2} \text{ and} \\
&\int_0^{l(t)} hU dx = h_0 U_0 l\int_0^1 FG d\xi
\end{aligned}\right\} \tag{17}$$

Using the relations in Eq. (17), integral Eqs. (15) and (16) are reduced to Eqs. (18) and (19) as below

$$\frac{d(h_0 l)}{dt}\int_0^1 F d\xi = h_0(t)U_0(t) \tag{18}$$

$$\frac{d\left(h_0 U_0 l\right)}{dt}\int_0^1 FG d\xi - h_0 U_0^2 - \frac{g h_0^2}{2} = -\frac{C_L h_0 U_0 l}{(1-C)}\int_0^1 FG d\xi \tag{19}$$

For the integral terms comprising similarity functions in above equations, following relations can be derived

$$\int_0^1 F d\xi = \frac{(2-B)}{2} = \eta \tag{20}$$

$$\int_0^1 FG d\xi = 1 - \frac{(A+B)}{2} + \frac{AB}{3} = \lambda \tag{21}$$

The integral models will be derived in the following section for each of the flow conditions considered that inherits both the IP and PD regime in its solution.

3.1 Integral model derivation for pressure inlet condition

While making use of the special condition that the inlet water depth remains constant i. e. $h(x = 0, t) = h_0$ (constant), Eqs (18) and (19) are changed into ordinary differential equations given by

$$\text{continuity:} \qquad \eta\frac{dl}{dt} = U_0(t) \tag{22}$$

$$\text{momentum:} \quad 2U_0^2 + l\frac{dU_0}{dt} = \frac{U_0^2}{\lambda} + \frac{g h_0}{2\lambda} - \frac{C_L U_0 l}{(1-C)} \tag{23}$$

Combining Eqs. (22) and (23), one can easily write the ODE for governing equation in terms of front position $l(t)$

$$\eta l\frac{d^2 l}{dt^2} + \left(2\eta^2 - \frac{\eta^2}{\lambda}\right)\left(\frac{dl}{dt}\right)^2 - \frac{g h_0}{2\lambda} = -\frac{C_L \eta l}{(1-C)}\frac{dl}{dt} \tag{24}$$

3.2 Integral model derivation for flux inlet condition

Using similar approach as done for pressure inlet condition except the special constant inflow flux condition as already mentioned, we arrive to get following continuity and momentum equations by integrating Eqs. (6) and (14) for the whole domain i.e. from $x = 0$ to $l(t)$

$$\text{continuity:} \qquad \eta\frac{d(h_0 l)}{dt} = q_0 \tag{25}$$

$$\text{momentum:} \quad \lambda\frac{dl}{dt} - \frac{q_0}{h_0} - \frac{g h_0^2}{2q_0} = -\frac{C_L \lambda l}{(1-C)} \tag{26}$$

Combining these two equations, we deduce single ordinary differential equation as follows for this condition

$$\frac{dl}{dt} = \frac{1}{\lambda}\left[\frac{\eta l}{t} + \frac{g q_0 t^2}{\eta^2 l^2}\right] - \frac{C_L l}{(1-C)} \tag{27}$$

4. Derivation of integral model for turbulent flow

For the case when quadratic resistance law is considered for high velocity flow through course porous media, we also have derived integral formulations. The governing equations for mass and momentum balance are given by Eqs. (6) and (7) in which the resistance coefficient in Eq. (3) is given by Eq. (5). Thus the momentum balance equation in its conservative form can be written as

$$\frac{\partial hU}{\partial t}+\frac{\partial hU^2}{\partial x}+g\frac{\partial}{\partial x}\left(\frac{h^2}{2}\right)=-\frac{C_T hU|U|}{(1-C)} \tag{28}$$

Integrating Eqs. (6) and (28) from $x = 0$ to $l(t)$ and making use of Leibnitz integral rule, we get following set of continuity and momentum equations

$$\frac{d(h_0 l)}{dt}\int_0^1 F d\xi = h_0(t)U_0(t) \tag{29}$$

$$\frac{d\left(h_0U_0l\right)}{dt}\int_0^1 FGd\xi - h_0U_0^2 - \frac{gh_0^2}{2} = -\frac{C_T h_0 U_0^2 l}{(1-C)}\int_0^1 FG^2 d\xi \tag{30}$$

To convert these equations into ordinary differential equations using same similarity distribution functions F and G we need one extra integral in addition to those given by Eqs. (20) and (21) i.e.

$$\int_0^1 FG^2 d\xi = 1-\frac{(2A+B)}{2}+\frac{(A^2+2AB)}{3}-\frac{A^2B}{4}=\psi \tag{31}$$

Hence, continuity and momentum equations are reduced to ordinary differential equations that are solved as initial value problems. The results for different boundary conditions are given below.

Pressure inlet condition

For the condition considered, Eqs. (29) and (30) reduce to

$$\eta\frac{d(h_0 l)}{dt}=h_0U_0$$

and
$$\lambda\frac{d\left(U_0 l\right)}{dt}-U_0^2-\frac{gh_0}{2}=-C_T\psi\left(U_0^2 l\right) \tag{32}$$

Combining these equations we get,

$$\frac{U_0^2}{\eta}+l\frac{dU_0}{dt}=\frac{1}{\lambda}\left[U_0^2+\frac{gh_0}{2}\right]-\frac{C_T\psi U_0^2 l}{\lambda} \tag{33}$$

which is solved for U_0 by Runge-Kutta method in this paper.

Flux inlet condition

The ordinary differential equation for for this condition can be derived from Eqs. (29) and (30) as

continuity:
$$\eta\frac{d(h_0 t l)}{dt}=q_0 \quad \text{and}$$

momentum:
$$\lambda\frac{dl}{dt}-\frac{q_0}{h_0}-\frac{gh_0^2}{2q_0}=-C_T\psi l U_0 \tag{34}$$

Again combining these two we get,

$$\lambda\frac{dl}{dt}-\frac{\eta l}{t}-\frac{gq_0t^2}{2\eta^2 l^2}=-C_T\psi l U_0 \tag{35}$$

5. Solution of integral model formulations

The governing nonlinear partial differential equations have been changed into ordinary differential Eqs. (24) and (27) for laminar flow where the linear resistance is considered, by similarity transformation technique. Also considering quadratic resistance law Eqs. (33) and (35) are derived. The value of constant coefficients η, λ and ψ are determined for A = -1.0 and B = 1.0 as already derived in our previous work[2] for similarity solution. We assume these constants do not change significantly for inertia-pressure and pressure-drag regimes. To solve these ODE's, we follow an iterative procedure using appropriate initial value. A well known fourth order Runge-Kutta method[7] is implemented. All other parameters like velocity and depth at the boundaries can be found after the non-linear ODE is solved for its dependent variable. The overall process can be found from any text book dealing with nonlinear ordinary differential equation. Only the results are shown in section 8 for the compactness.

6. Outline of Laboratory tests

Laboratory experiments were carried out for the evaluation of both the proposed integral and numerical models. A rectangular transparent perspex flume filled with glass beads as porous media was used. In the experiment glass beads of diameter 1mm, 5mm and 12mm, taken separately, were used as porous media under constant water depth at the leftmost boundary so as to simulate case A. The summary of laboratory tests is given in the table 2. To begin with the experiment, a vertical gate at the inlet is pulled up instantaneously with the help of a nylon rope so as to make it as instantaneous as possible. Such an arrangement for the experiment is given in Fig. 3. The velocity and depth of flow with free surface are taken using a digital movie camera placed near the side of the flume. The position of front and depth distribution for different time is traced by the image interpretation with the help of grids drawn at 50mm interval on the perspex plate of the flume facing the camera. The time dependence and the flow profile of the intrusion behavior observed during the experiment are compared with the analytical solution and numerical simulations as well.

Table 2. Laboratory test cases

Test name	Bead size	Hydraulic conductivity	Remarks
Expt I.	1 mm	K= 0.01 m/s	Case A: h_0= 0.085m ; C = 0.6
Expt II.	5 mm	K= 0.10 m/s	
Expt III.	12 mm	K= 0.20 m/s	

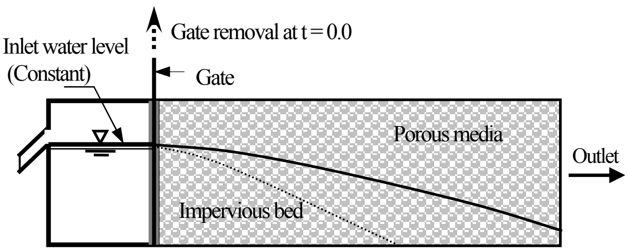

Fig. 3 Schematic layout of the experimental set up

The experiment was carried out until a steady state condition was attained. The permeability was also calculated using the hydraulic gradient when the system attained steady state. The measured steady state discharge and the flow depths have been used for the calculation of the permeability of the media for use in numerical simulation. For multi-sized natural soils, the average hydraulic properties can be expressed in terms of intrinsic permeability (k) and porosity (ε) of the media.

Table 3. List of numerical runs

Numerical run	Bead size	Hydraulic conductivity	Remarks
RUN 1	1mm	$K = 0.01$ m/s	Case A : $C = 0.6, h_0 = 0.085$m
RUN 2	5mm	$K = 0.1$ m/s	
RUN 3	12mm	$K = 0.2$ m/s	
RUN 4	5mm	$K = 0.1$ m/s	Case B: $C = 0.6$, $q_0 = 0.005$m^3/s per m

7. Numerical Simulation

This section explains about the algorithm adopted for the unsteady free-surface flow through the porous media. A number of vertical two dimensional numerical simulations are carried out as shown in table 3.

7.1 Governing equations

The free surface flow of viscous and incompressible fluid in porous media is governed by a set of continuity and momentum equation given by Navier-Stokes equations extended with porous drag resistance terms as below

$$\frac{\partial (1-C)u_i}{\partial x_i} = 0 \tag{36}$$

$$\frac{\partial (1-C)u_i}{\partial t} + \frac{\partial (1-C)u_i u_j}{\partial x_j} = (1-C)g_i - \frac{(1-C)}{\rho}\frac{\partial p}{\partial x_i} + \nu \frac{\partial^2 (1-C)u_i}{\partial x_j \partial x_j} + \frac{R_i}{\rho} \tag{37}$$

where u_i is the velocity vector, also called the pore water velocity in the porous medium, C is the volumetric concentration of the solids in the porous medium, R_i is the flow resistance term due to porous matrix, p is the pressure and ν is the kinematic viscosity of the fluid. The model can account the spatial variability of permeability and porosity. The above equations can also be used for anisotropic porous media and for variable porosity. According to the volume averaging procedure[9], the Darcy's flux is equal to the product of actual pore fluid velocity as used in above expressions and the porosity of the medium given by

$$V_i = (1-C)u_i \tag{38}$$

where V_i denotes the Darcy's flux. The total drag resistance due to the presence of the solid particles per unit volume R_i in the momentum balance equation represents the sum of the pressure drag and viscous friction. The total drag resistance force per unit volume of the fluid for a wide range of flow as expressed by Ergun's correlation[10] can be written as

$$\frac{R_i}{\rho} = -\left[\frac{\nu (1-C)^2 u_i}{k} + \frac{F_{ch}(1-C)^3 u_i |u_i|}{\sqrt{k}}\right] \tag{39}$$

where k and F_{ch} are the permeability in m^2 and the Forchheimer's inertia factor. For a randomly packed bed of spheres such coefficients can be expressed in terms of the solid concentration C and the mean diameter of the particles d_p in the porous medium as

$$k = \frac{(1-C)^2 d_p{}^2}{150 C^2} \quad \text{and} \quad F_{ch} = \frac{1.75}{\sqrt{150}\sqrt{(1-C)^3}} \tag{40}$$

It should be noted that the Eqs. (36) and (37) governing the flow in porous media is very much similar to the classical continuity and Navier-Stokes equations for the open channel flow. The equations can also be used in free domain by switching suitably the values of C and k. In doing so, the terms used for the drag resistance of the solid matrix will be vanished outside the porous media which eventually results the equation for the flow in free domain. In Eq. (39), the first term represents linear (Darcy) resistance whereas the second term represents quadratic resistance term. The contribution of second term vanishes automatically when the velocities are small. These resistance terms were taken separately in Eq. (3) for the theoretical analysis.

The depth averaged form of Eqs. (36) and (37) are already used in section 2.1 as Eqs. (6) and (7) in which the viscous stress terms are neglected. If we nondimensionalize Eq. (37) by scaling the velocity by hydraulic conductivity (K) and the spatial coordinate by mean diameter (D) of the particle, we get,

viscous term $= \dfrac{\nu K(1-C)}{D^2}\dfrac{\partial^2 u_i^*}{\partial x_i^* \partial x_i^*}$

and, porous media drag term $= g(1-C)u_i^*$,

where nondimensional velocity, $u_i^* = u_i / K$ and non dimensional spatial coordinate, $x_i^* = x_i / D$. From this nondimensional analysis, it is known that the relative significance of viscous term is very low because it is obtained that $\nu K(1-C)/D^2 \ll g(1-C)$. So to simplify the theoretical analysis, we neglected the stress term and retained porous media drag term in Eq. (2).

7.2 Boundary condition and free surface evolution

Both for the two cases studied here, the left inlet boundary is treated as Dirichlet boundary condition where either a pressure due to water pool or the prescribed flux is supplied depending upon the case considered. At the bottom of the channel the slip condition is applied to simulate the smooth perspex surface. The downstream boundary is treated as a Neumann type where zero gradient condition for velocity and pressure is applied to ensure the continuation of the flow. At the free surface of the flow, the atmospheric pressure condition is applied. But the free surface evolution inside the porous media is not known a priory, rather is a part of the solution, an important feature of this study. The method introduces a volume of fluid (VOF) function to define the water region and its saturation within the cell. The evolution of the free surface is traced using VOF method which is discussed in the subsequent section.

Evolution of Free Surface

Consider a function f which represents the fractional cell saturation defined in a continuous domain as

$$f = \begin{cases} 1 & \text{for full cell} \\ 0 & \text{for empty cell} \\ 0\sim 1 & \text{for surface cell} \end{cases} \tag{41}$$

For a cell (i,j) of volume $V_{i,j}$, a volume function $f_{i,j}$, is defined as

$$f_{i,j} = \frac{1}{(1-C)V_{i,j}} \int_{V_{i,j}} f\, dV \tag{42}$$

where dV = (1-C)$dxdy$. The time evolution of the free surface flow inside the porous domain is governed by the following equation.

$$\frac{\partial f}{\partial t}+\frac{\partial (u_j f)}{\partial x_j}=0 \tag{43}$$

where f represents the fractional saturation of fluid within a cell. Eq. (43) is the material derivative of the saturation volume f of fluid within a cell[11, 12]. This equation is solved after the velocity field is updated because the position of fluid surface cannot be known a-priory. Given the volumetric nature of function f and in order to maintain a sharp interface, the discretization of Eq. (43) requires a special treatment. The donor-acceptor concept[13] along with MUSCL type TVD[14] scheme is used for the non-oscillatory convection of the VOF function.

7.3 Solution algorithm by CIP method

In this section we present the solution algorithm in vertical 2D simulation for the flow in channel filled with porous media, but its extension to 3D is straightforward. Governing Eqs. (36) and (37) are solved numerically on a uniform staggered Cartesian grid by finite volume method. The cubic interpolation polynomial (CIP) method[15, 16] is adopted as the base scheme for the numerical solution. The basic idea of the CIP method is that for advection computation of any flow variable, not only the transportation equation but also the transportation equation of its spatial gradients are solved. The equations are written here in vector notation for compactness. Referring to the momentum equation (37), its spatial derivatives can be written as

$$\begin{aligned}\frac{\partial(1-C)\mathbf{u}_x}{\partial t}+((1-C)\mathbf{u}\bullet\nabla)\mathbf{u}_x&=-(\mathbf{u}_x\bullet\nabla)(1-C)\mathbf{u}\\&-(1-C)\nabla p_x+\nu(1-C)\nabla^2\mathbf{u}_x+\frac{\mathbf{R}_x}{\rho}\end{aligned} \tag{44}$$

$$\begin{aligned}\frac{\partial(1-C)\mathbf{u}_y}{\partial t}+((1-C)\mathbf{u}\bullet\nabla)\mathbf{u}_y&=-(\mathbf{u}_y\bullet\nabla)(1-C)\mathbf{u}\\&-(1-C)\nabla p_y+\nu(1-C)\nabla^2\mathbf{u}_y+\frac{\mathbf{R}_y}{\rho}\end{aligned} \tag{45}$$

where the density is absorbed in the pressure term itself and ν is the kinematic viscosity of fluid. The subscripts x and y denote the spatial derivatives with respect to x and y directions respectively. The governing equations are split into two steps: non-advection and advection phase. The non-advection phase is solved by the conventional central finite difference scheme whereas the advection phase is solved by the CIP method. To use CIP method, we consider transient conditions in Eqs. (36) and (37). Then to reach a steady state, we continue the calculation until the solution is at steady state. Thus applying the fractional time step approach, the numerical solution of the governing equations can be divided into the following two steps

(1) The non-advection phase

The governing equations for the non-advection phase are

$$\begin{aligned}(1-C)\frac{\hat{\mathbf{u}}-\mathbf{u}^n}{\Delta t}&=-(1-C)\nabla p\\&+\nu(1-C)\nabla^2\mathbf{u}^n+\mathbf{g}(1-C)+\frac{\mathbf{R}}{\rho}\end{aligned},$$

$$\begin{aligned}(1-C)\frac{\hat{\mathbf{u}}_x-\mathbf{u}_x^n}{\Delta t}&=-((1-C)\mathbf{u}_x^n\bullet\nabla)\mathbf{u}^n\\&-(1-C)\nabla p_x+\nu(1-C)\nabla^2\mathbf{u}_x^n+\frac{\mathbf{R}_x}{\rho}\end{aligned} \quad \text{and}$$

$$\begin{aligned}(1-C)\frac{\hat{\mathbf{u}}_y-\mathbf{u}_y^n}{\Delta t}&=-((1-C)\mathbf{u}_y^n\bullet\nabla)\mathbf{u}^n\\&-(1-C)\nabla p_y+\nu(1-C)\nabla^2\mathbf{u}_y^n+\frac{\mathbf{R}_y}{\rho}\end{aligned} \tag{46}$$

In order to avoid considering the pressure derivatives p_x and p_y as nodal variables and updating them for each time step in the second and third equations in Eq. (46), the right hand side terms are replaced by the velocity terms from the first equation. Then, the second and third equations can be written as

$$(1-C)\frac{\hat{\mathbf{u}}_x-\mathbf{u}_x^n}{\Delta t}=-((1-C)\mathbf{u}_x^n\bullet\nabla)\mathbf{u}^n+\frac{\partial}{\partial x}\left(\frac{\hat{\mathbf{u}}_x-\mathbf{u}_x^n}{\Delta t}\right) \quad \text{and}$$

$$(1-C)\frac{\hat{\mathbf{u}}_y-\mathbf{u}_y^n}{\Delta t}=-((1-C)\mathbf{u}_y^n\bullet\nabla)\mathbf{u}^n+\frac{\partial}{\partial y}\left(\frac{\hat{\mathbf{u}}_y-\mathbf{u}_y^n}{\Delta t}\right) \tag{47}$$

(2) The advection phase

The equations to be solved in a typical time step in this phase are written as

$$(1-C)\frac{\mathbf{u}^{n+1}-\hat{\mathbf{u}}}{\Delta t}+((1-C)\hat{\mathbf{u}}\bullet\nabla)\hat{\mathbf{u}}=0\ ,$$

$$(1-C)\frac{\mathbf{u}_x^{n+1}-\hat{\mathbf{u}}_x}{\Delta t}+((1-C)\hat{\mathbf{u}}\bullet\nabla)\hat{\mathbf{u}}_x=0 \quad \text{and}$$

$$(1-C)\frac{\mathbf{u}_y^{n+1}-\hat{\mathbf{u}}_y}{\Delta t}+((1-C)\hat{\mathbf{u}}\bullet\nabla)\hat{\mathbf{u}}_y=0 \tag{48}$$

where n denotes the beginning of the step, and $\hat{\mathbf{u}}$, $\hat{\mathbf{u}}_x$ and $\hat{\mathbf{u}}_y$ denote the velocity vector and its spatial derivatives at the end of the non-advection phase. The last two equations in Eq. (48) are the equations for updating the spatial derivatives of velocity.

First of all, the velocity after non-advection phase $\hat{\mathbf{u}}$ is calculated using the conventional central finite difference scheme from the first equation in Eq. (46) and so for the spatial derivatives using Eq. (47). Then new time step velocity $\mathbf{u}^{n+1}$ is obtained by applying a cubic interpolation polynomial to solve Eq. (48). In this phase, velocity and its spatial derivatives obtained after non-advection phase are used. Also spatial derivatives are updated for use in the next time step. Iteration is made until the divergence of the velocity field, $\nabla\bullet(1\text{-}C)\mathbf{u}^{n+1}$, is diminished to some prescribed value so as to satisfy the continuity Eq. (36). Then we get the updated pressure. An iterative procedure similar to HSMAC type iteration algorithm[12] is implemented to update the velocity vector and the pressure. Thus the calculations for one time step are now complete. For the next time step, we take the values $\mathbf{u}^{n+1}$, p^{n+1}, $\mathbf{u}_x^{n+1}$ and $\mathbf{u}_y^{n+1}$ to the next time step non-advection phase and repeat the calculations.

8. Results and discussion

As depicted in the theoretical derivation considering the similarity distributions of variables following plots clearly show the two flow regimes in the flow through porous medium for both linear and quadratic resistance law. Following are the results of the integral model which represent early inertia-pressure regime followed by pressure-drag regime.

Integral model results for linear resistance law

Figs. 4(a) and (b) show a log-log plot of front position and water entry velocity respectively with respect to time for case A. The early

IP regime is followed by PD regime with smooth transition. The transition time for the regime change highly depends upon the characteristics porous media. The K values shown on the plots are the hydraulic conductivity (m/s) of porous media. The temporal powers measured from the plots itself are shown on the plots to compare it with the results presented in table 1 and it matches well. It is to be noted here that there is the dominance of PD regime in the flow for low permeable medium. In Fig. 4(a), the slope of the plot is found exactly what is derived in the theory. Initial value $c = 1$ represents IP regime whereas $c = 1/2$ represents PD regime. Similarly in Fig. 4(b), there is constant inflow velocity initially during IP regime and then it decreases with -1/2 power of time during PD regime. The transition from IP to PD regime can be seen very smooth.

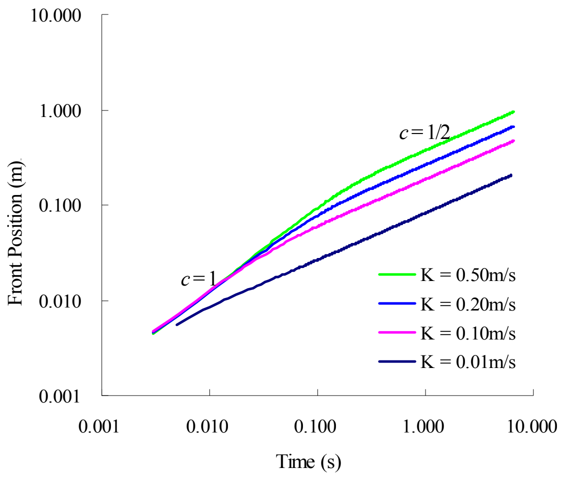

4 (a)

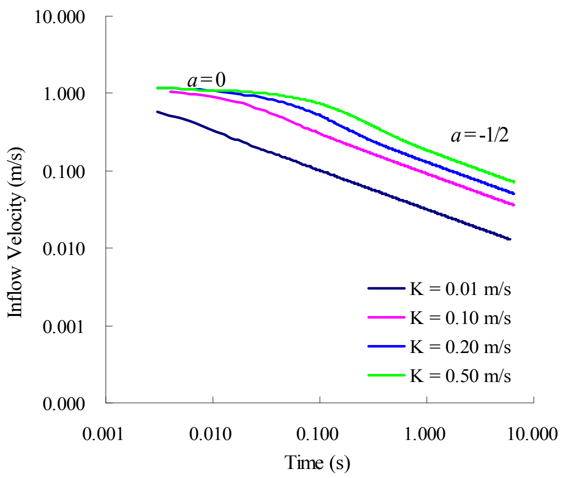

4 (b)

Fig. 4 Temporal values of (a) front position (b) entry velocity. (case A: h_0 =0.085m)

Following figures are the results of the solution for integral formulation derived for case B. Figs. 5(a)-(c) show the plots of front position, depth at the origin and entry velocity with respect to time respectively. The plots show two flow regimes in the intrusion process. The early impulsive IP regime is followed by relatively milder velocity PD regime. The transition from early IP regime to PD regime is smooth and its occurrence time is highly dependent on the porous media characteristics. We can observe the longer dominance of IP regime in the case of highly permeable porous media. Also there is a clear shift of the transition time as the permeability value increases. The values of measured temporal powers are shown on the plot and they are matching with what derived from similarity analysis.

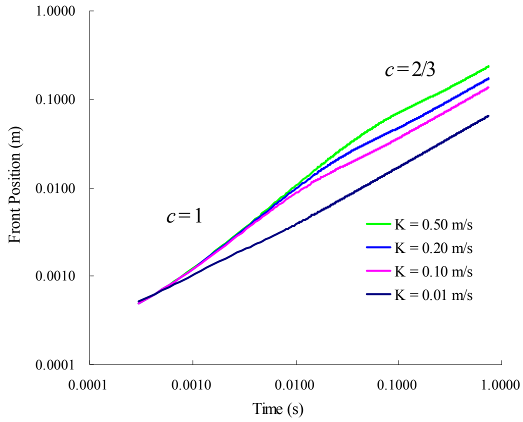

5 (a)

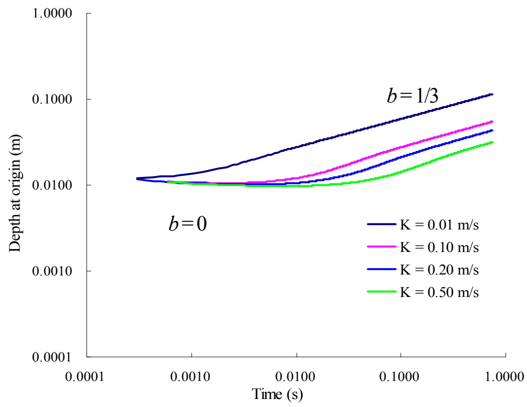

5 (b)

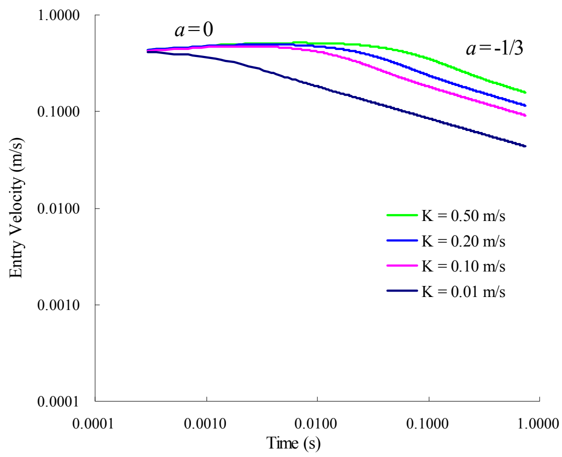

5 (c)

Fig. 5 Temporal values of (a) front position (b) depth at origin (c) entry velocity. (case B: $q_0 = 5\times10^{-03}$ m^3/s per m)

The main difference in case B is the increment of depth at origin (or entry depth) with time in PD regime [see Fig. 5(b)] which was always constant for case A. The pore Reynolds number in the case of very low permeable media [e.g. K = 0.01m/s] is calculated below 10 and it goes on increasing with hydraulic conductivity up to Re_p= 500. Both inertia-pressure and pressure-drag affect the flow dynamics but flow is still laminar according to the classification shown in section 1.

Integral model results of quadratic resistance law

Following plots are the results of integral model for the turbulent flows where quadratic resistance law is considered. For this case, pore Reynolds number for turbulent flow is more than 500 and thus quadratic (or square law) is applicable. Figs. 6(a) and (b) show the plots for front position and entry velocity with respect to time for pressure inlet condition. The CT value (C_T) shown on the plots are the inertial coefficients for the square (or quadratic) law consideration. The higher C_T values mean the low permeable porous media. The temporal powers derived are in good agreement with the results of integral models.

Fig. 7(a)-(c) show the plots for the turbulent flow with inflow flux boundary condition. In this case also the integral model represents both the flow regimes. The measured values of temporal powers *a*, *b* and *c* are also shown on the figures. They are in good agreement with the theoretical derivations.

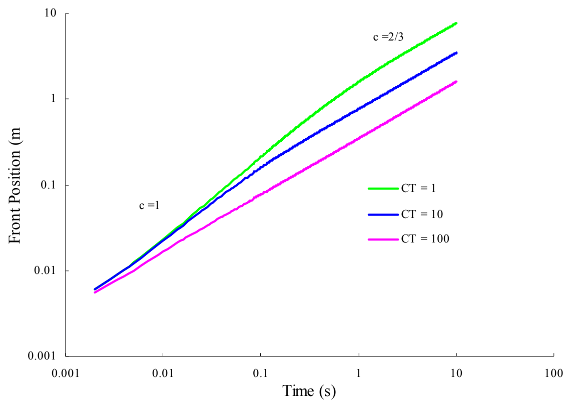

6 (a)

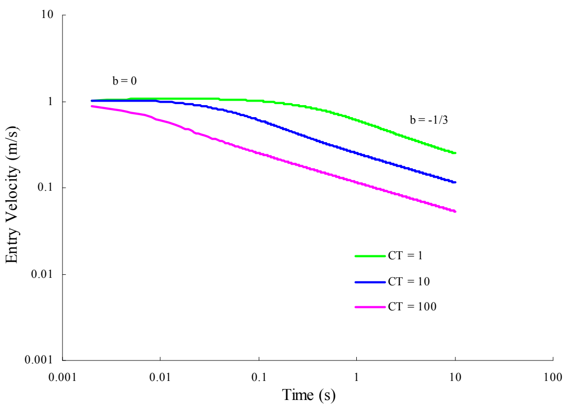

6 (b)

Fig. 6 Temporal values of (a) front position (b) entry velocity. (case A: quadratic law : h_0 =0.085m)

Results from numerical simulation and experiments

In Fig. 8 and 9, simulated flow profile showing velocity vector and corresponding flow profile observed during the experiment are shown. The results shown here are for 1mm glass beads. A constant water level of 0.085m was maintained at the upstream boundary of

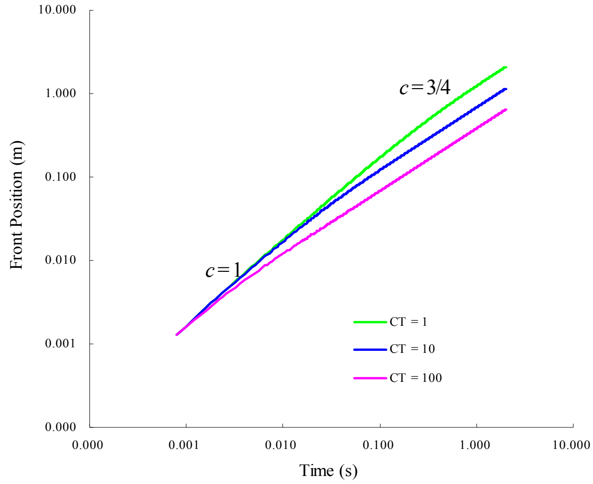

7 (a)

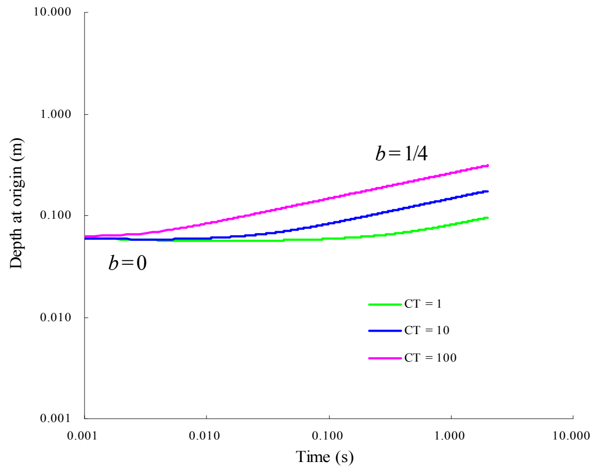

7 (b)

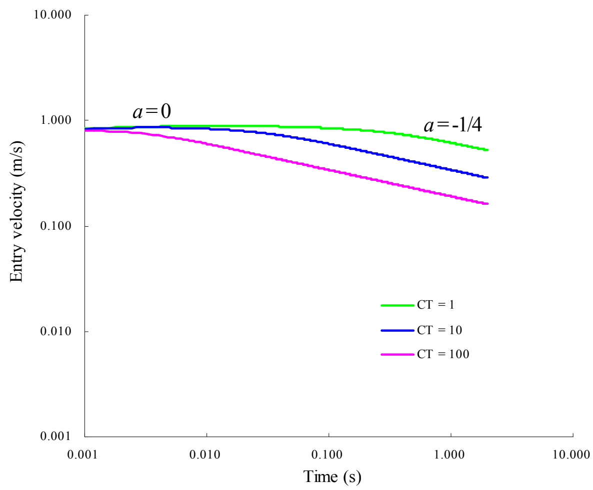

7(c)

Fig. 7 Temporal values of (a) front position (b) depth at origin (c) entry velocity. (case B, square law : q_0 =5×10^{-03} m^3/s per m) the channel filled with porous media. The result shows a close agreement between the experiment and numerical simulation.

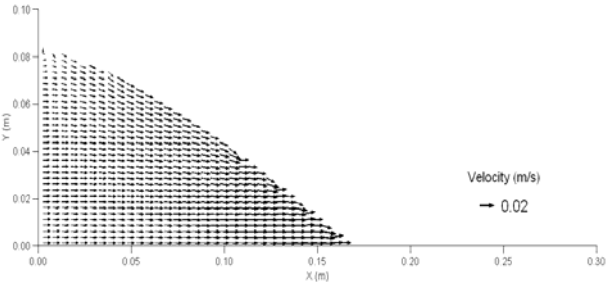

8 (a)

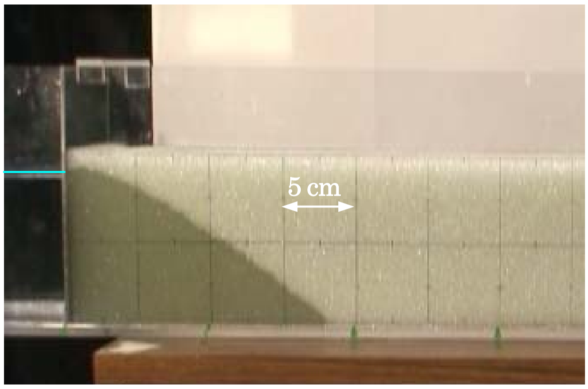

8 (b)

Fig. 8 Flow profile at t = 5s (a) simulation (b) experiment [Expt I.]

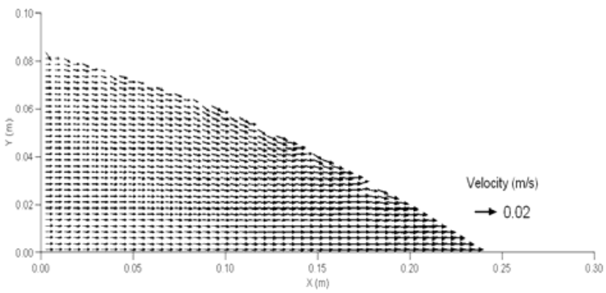

9 (a)

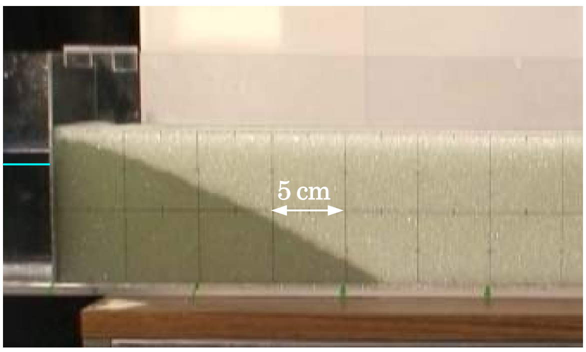

9 (b)

Fig. 9 Flow profile at t = 10s (a) simulation (b) experiment [Expt I.]

Comparative results from numerical simulation, integral models and experiment

In the figures below plots for the flows in porous media having different size and hydraulic conductivity are shown. The position of front in the unsteady free-surface flow inside porous media obtained from integral formulation, numerical simulation and experiment are shown. Fig. 10, 11 and 12 show a comparison plot of temporal front position as obtained from the numerical run, integral model and the experiment in normal and log-log graphs for porous media of diameters 1mm, 5mm and 12mm respectively. It is also noticed here the PD regime is distinctly dominant for the flow in 1mm glass beads owing to its low permeability value. The discrepancy is very slight in the case of 5mm diameter porous media. For the case 12 mm diameter glass bead [see Fig.12], the integral model results are highly confirmative to the square law. The experimentally measured pore Reynolds number was also higher than 500 owing to its high permeability. Square law for the intrusion through porous media holds good for the porous media of large permeability. The discrepancy in the case of 5mm bead are in the early periods might be due to the non confirming similarity distribution of depth in the very early stage, error in the experimental timing etc. However the nonlinear natures of the phenomena are clearly depicted by these integral models. There are some discrepancies in the integral model results in the initial time stages but for the later time stages it shows satisfactory results. This may be due to the non-confirming similarity distribution of depth and velocity in very early stage of intrusion; further research is needed to improve the results in the early stage.

Fig. 13 shows a plot for the front position for case B i.e. for flux inlet condition. The results from the integral model and numerical simulation are in good agreement. Integral model results presented here uses linear resistance law. Thus in the case of flux inlet boundary also the spatial integral models work well.

9. Summary and conclusions

Free-surface transient flow through porous media has been analyzed for two different inlet conditions. It is pointed out that there are two flow regimes in the intrusion process of fluid into the porous media. An integral formulation for unsteady depth distribution, velocity and front speed under constant water level and constant flux discharge inlet conditions have been developed from similarity law. Analysis is done for both laminar and turbulent flows. The formulation presented provides additional analytical insight about the intrusion dynamics. In addition, the method proposed can be successfully used for the solution of a host of other nonlinear problems that admit self-similarity. The developed solutions for constant inlet water level condition have been verified with the experimental observation. The unsteady distributions of drainage depth, inflow velocity and front speeds have been compared for various porous media characterized by its corresponding permeability.

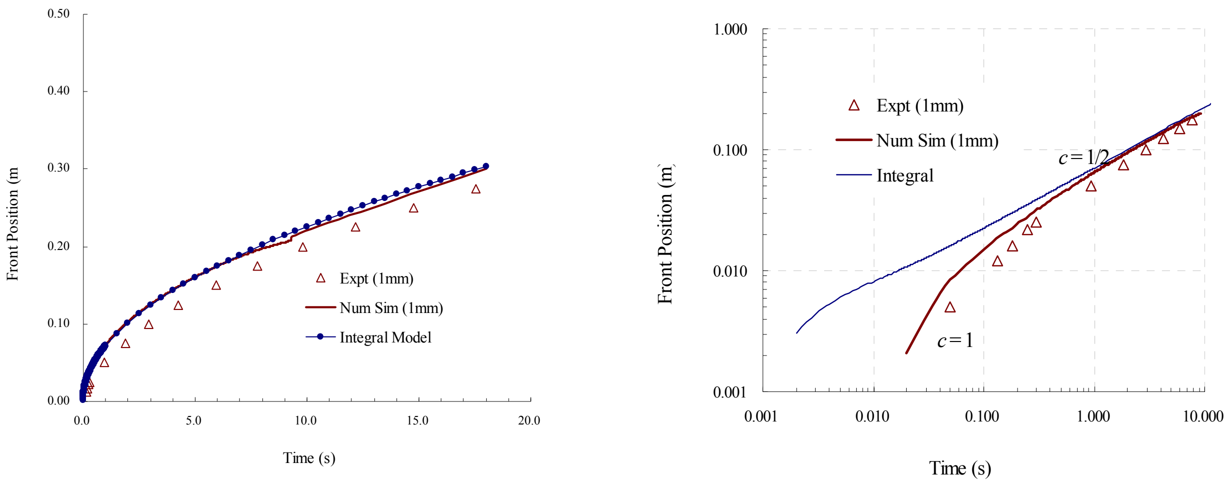

10 (a) 10 (b)

Fig. 10 Temporal front position (a) normal plot (b) log-log plot (1mm glass bead)

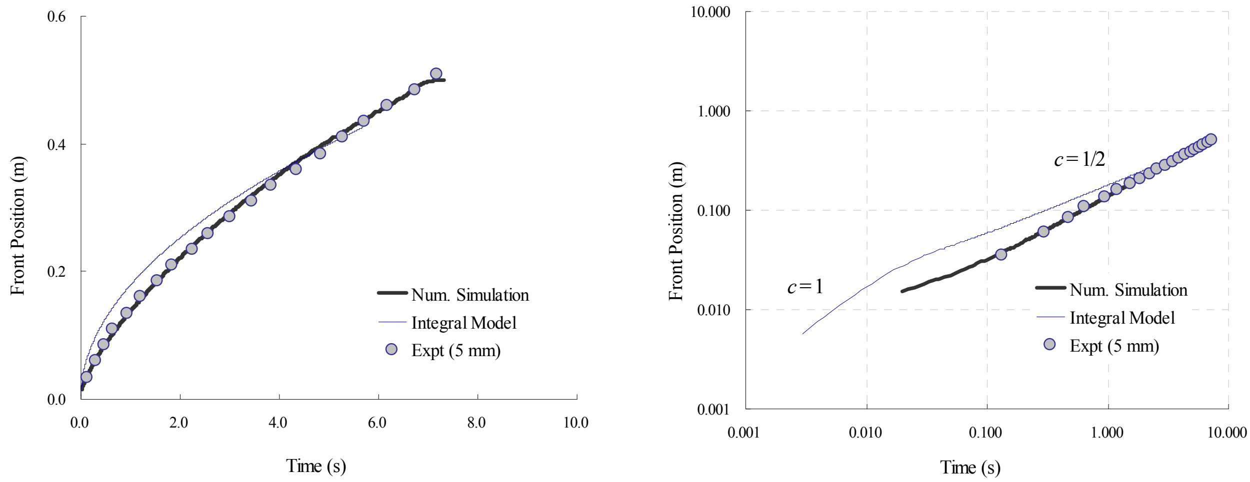

11 (a) 11 (b)

Fig. 11 Temporal front position (a) normal plot (b) log-log plot (5mm glass bead)

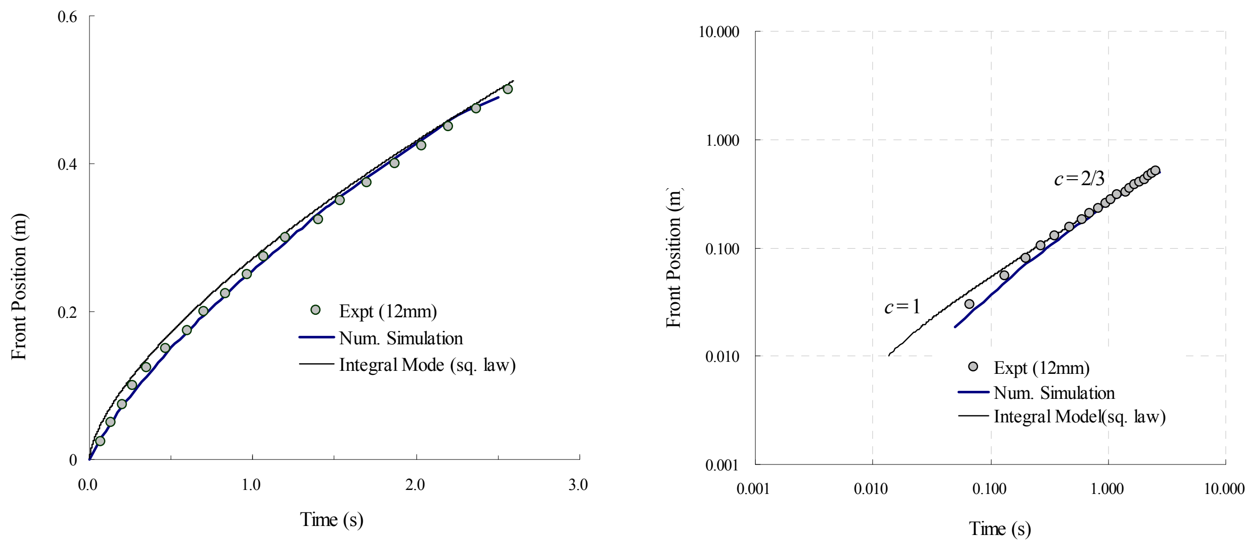

12 (a) 12 (b)

Fig. 12 Temporal front position (a) normal plot (b) log-log plot (12mm glass bead)

The analysis indicates that the integral model clearly represents the nonlinear flow behavior in the porous media both in laminar and turbulent flow conditions. The integral model results are in agreement with those obtained by similarity solution for the temporal change of velocity, depth at the origin and front positions. A numerical simulation algorithm in vertical 2D unsteady free surface flow through porous media is described. The algorithm uses a finite volume approach to simulate such non-Darcy inertial free-surface fluid flow. The mathematical formulation makes use of CIP method along with HSMAC type pressure solver to simulate the free surface flow through porous media. The free surface evolution inside the porous media is traced by the pure convection of a scalar function called volume of fluid function, or sometime called color function, with the modification for use in porous media. The free surface profiles well matches with the experimental results. The numerical scheme has thus been verified by comparing its results against those of analytical methods and experimental observations.

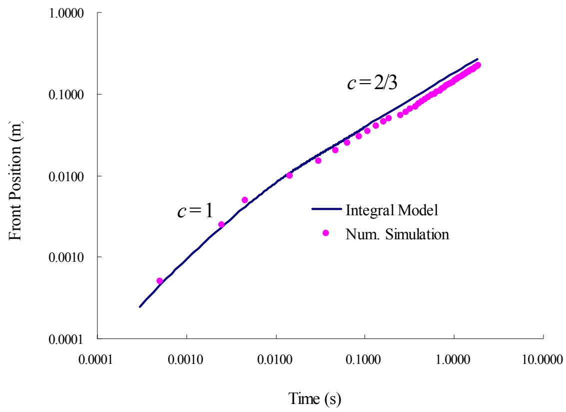

Fig. 13 Position of front versus time (case B: $q_0 = \mathrm{m}^3/\mathrm{s}$ per m, K= 0.1 m/s) [RUN 4]

In the high velocity flow through porous media, the accurate free surface tracing is a challenging task for such unsteady flow problems. The VOF method is implemented with some adaption for use in porous media and the results show very satisfactory free surface configuration. Also the use of CIP method is also advantageous over conventional schemes because CIP method advects the variable and its spatial derivative as well. Hence the numerical diffusion is reduced giving rise to a sharp interface[17] in this method. From the present results, it can be concluded that two dimensional mathematical model gives better result and understanding of the intrusion process. With such multidimensional approach, the free surface flow dynamics through the porous media is described at every point in the space and time. On the other hand, the integral model is useful for quick assessment of the flow variables at the boundaries of the flow domains with homogeneous porous media characteristics. It can be useful for simple rectangular domains and for the transient phenomenon which admits self-similar solutions.

References

1) Hlushkou, D., Tallarek, U., Transition from creeping via viscous-inertial to turbulent flow in fixed beds, *J. Chromatography*, *Elsevier*, Vol.1126, pp.70-85, 2006.
2) Ghimire, B., Hosoda, T. and Nakashima, S., An investigation on lateral intrusion process of water into porous media under different upstream boundary conditions, *J. Applied Mech.*, JSCE, Vol.10, pp.839-846, 2007.
3) Hosoda, T., Kokado, T. and Miyagawa, T., Flow characteristics of viscous fluids on the basis of self-similarity law and its applications to high flow concrete, *J. Applied Mech.*, JSCE, Vol.3, pp.313-321, 2000.
4) Huppert, H. E., The propagation of two-dimensional and axisymmetric viscous gravity currents over a rigid horizontal surface, *J. Fluid Mech.*, Vol.121, pp.43-58, 1982.
5) Barenblatt, G. I. and Vazquez, J. L., A new free boundary problem for unsteady flows in porous media, *Euro. J. Applied Maths.*, Vol.9, pp.37-54, 1998.
6) Huppert, H. E. and Woods, A. W., Gravity-driven flows in porous layers, *J. Fluid Mech.*, Vol.292, pp.55-69, 1995.
7) Chen, Z. X. and Bodvarsson, G. S., Witherspoon, E. A., Yortsos, Y. C., An integral equation formulation for the unconfined flow of groundwater with variable inlet conditions, *Transport in Porous Media*, Vol.18, pp.15-36, 1995.
8) Press, W. H., Teukolsky, S. A., Vetterling, W. T., Flannery, B. P., *Numerical recipes, second ed.*, Cambridge University Press, 1996.
9) Hsu, C. T. and Cheng, P., Thermal dispersion in a porous medium. *Int. J. Heat and Mass Transfer*, Vol.33(8), pp.1587-1597, 1990.
10) Ergun, S., Fluid flow through packed columns, *Chem. Engng. Prog.*, Vol.48, pp.89-94, 1952.
11) Hur, D. S. and Mizutani N., Numerical estimation of the wave forces acting on a three dimensional body on submerged breakwater, *Coastal Eng. J.*, Vol.47, pp.329-345, 2003.
12) Jacimovic, N., Hosoda, T., Kishida, K. and Ivetic, M., Numerical Solution of the Navier-Stokes equations for incompressible flow in porous media with free surface boundary, *J. Applied Mech.*, JSCE, Vol.8, pp.225-231, 2005.
13) Hirt, C. W. and Nichols, B. D., Volume of fluid (VOF) method for the dynamics of free boundaries, *J. Comput. Phys.*, Vol.39, pp.201-225, 1981.
14) Van Leer, B., Towards the ultimate conservative difference scheme, *J. Comput. Phys.*, Vol.32, pp.101-136, 1979.
15) Yabe, T. and Aoki, T., A universal solver for hyperbolic equations by cubic-polynomial interpolation I: One dimensional solver, *Comput. Phys. Commun.*, Vol.66, pp.219-232, 1991.
16) Yabe, T., Ishikawa, T., Wang, P. Y., Aoki T, Kadota, Y and Ikeda F., A universal solver for hyperbolic equations by cubic-polynomial interpolation II: Two and three dimensional solvers, *Comput. Phys. Commun.*, Vol.66, pp.233-242, 1991.
17) Yabe, T., Xiao, F. and Utsumi, T., The constrained interpolation profile method for multiphase analysis, *J. Comput. Phys.*, Vol.169, pp.556–593, 2001.

(Received: April 9, 2009)